

# NEURAL NETWORK BASED POINT SPREAD FUNCTION DECONVOLUTION FOR ASTRONOMICAL APPLICATIONS

HONG WANG<sup>1</sup>, SREEVARSHA SREEJITH<sup>2</sup>, YUEWEI LIN<sup>1</sup>, NESAR RAMACHANDRA<sup>3,4</sup>, ANZE SLOSAR<sup>2</sup>, AND SHINJAE YOO<sup>1</sup>

<sup>1</sup> Computational Science Initiative, Brookhaven National Laboratory, Upton, NY 11973

<sup>2</sup> Physics Department, Brookhaven National Laboratory, Upton, NY 11973

<sup>3</sup> Computational Science Division, Argonne National Laboratory, Lemont, IL, USA and

<sup>4</sup> High Energy Physics Division, Argonne National Laboratory, Lemont, IL, USA

*Version October 5, 2022*

## ABSTRACT

Optical astronomical images are strongly affected by the point spread function (PSF) of the optical system and the atmosphere (seeing) which blurs the observed image. The amount of blurring depends both on the observed band, and more crucially, on the atmospheric conditions during observation. A typical astronomical image will therefore have a unique PSF that is non-circular and different in different bands. Observations of known stars give us a determination of this PSF. Therefore, any serious candidate for production analysis of astronomical images must take the known PSF into account during the image analysis. So far the majority of applications of neural networks (NN) to astronomical image analysis have ignored this problem by assuming a fixed PSF in training and validation. We present a neural network based deconvolution algorithm based on Deep Wiener Deconvolution Network (DWDN) that takes the PSF shape into account when performing deconvolution as an example of one possible approach to enabling neural network to use the PSF information. We study the performance of several versions of this algorithm under realistic observational conditions in terms of recovery of most relevant astronomical quantities such as colors, ellipticities and orientations. We also investigate the performance of custom loss functions and find that they cause modest improvements in the recovery of astronomical quantities.

## 1. INTRODUCTION

The advent of large telescopes and big data sets are bringing about a transformative era for astronomical survey science. New datasets obtained from upcoming ground-based and space-based observing facilities will extract data from large volumes of the observable sky at unprecedented depths and cadences. An important addition to the large array of data observed using ground-based observatories will be the Legacy Survey of Space and Time (LSST) from the Vera Rubin Observatory (LSST Science Collaboration et al. 2009), adding to existing datasets from the Dark Energy Survey (DES, Abbott et al. 2018) and Hyper-Suprime Cam (HSC, Hikage et al. 2019). We also expect upcoming space-based surveys such as Euclid (Refregier et al. 2010) and Nancy Grace Roman telescope (Green et al. 2012) to add on to this data influx and produce excellently uniform datasets. While the resolution of space-based telescopes is usually diffraction limited, large aperture ground based survey telescopes are limited by seeing. Seeing is a distortion of the image caused by the perturbation of an optical wavefront as it passes through the turbulent atmosphere and results in a finite point-spread function (PSF). Due to the large field of view, these surveys will not be able to employ adaptive optics resulting in an arcsecond sized PSF.

The two main features of the PSF is that it is variable, because the atmosphere above the telescope is variable. It varies both in size, shape and orientation. It is typically asymmetric and is different in different pass bands. On the other hand, it is also known in each exposure, because invariably every exposure contains stars that are excellent point sources and therefore can be used to directly probe the PSF.

In astronomical image analysis we want to recover the unbiased estimates of the object intrinsic parameters, such as their shapes, positions and fluxes in the presence of noise and varying PSF. Machine learning techniques hold promise for speeding up these processes. Several machine learning based methods have been proposed recently that use neural networks for astronomical image analysis. These mostly grapple with the galaxy deblending problem. Reiman & Göhre (2019) designed a branched deblender with generative adversarial networks, which can work on the deblending of images with two overlapped galaxies. Boucaud et al. (2020) developed a framework for measuring the photometry of blended galaxies as well as perform segmentation with a standard convolutional neural network (CNN) and a U-Net. Arcelin et al. (2021) introduced an algorithm where a Variational Auto Encoder (VAE)-like neural network was used for galaxy deblending. We ourselves, have proposed an approach using residual dense neural networks (Wang et al. 2021).

Most of the current generation neural-network based galaxy deblenders assume a number of simplifying assumptions, including a constant PSF. This problem is usually “swept under the rug” by assuming that several training sets can be provided, one for each PSF. However, this is likely impractical for reasons we will cover in the following sections. It is also clear that simply ignoring this problem will lead to biased and sub-optimally inferred parameters for individual objects. Therefore the proper treatment of the PSF is one of the few issues that need to be addressed before neural network based approaches can be lifted from the realm of toy problems to realistic approaches. Other issues include

blending, masking and various detector artifacts. In this work we specifically address the question of PSFs, and build a network that takes a noisy, convolved image of an astronomical object uses PSF information to deconvolve it and produce a true image of the galaxy at the resolution supported by the PSF.

## 2. DESCRIPTION OF THE PROBLEM

We use a simple linear model for the observed astronomical image, a convolution with a PSF followed by the addition of observational noise:

$$I_i = I_{gt,i} \circledast \text{PSF}_i + N_i, \quad (1)$$

where  $\text{PSF}_i$  is the PSF for the channel  $i$ ,  $N_i$  is the noise, assumed to be homogeneous and normally distributed and index  $gt$  that refers to the ground truth. It is important to note that PSF is band dependent and that the amplitude of noise is also band-dependent. This model is not strictly true because the detector effects such as brighter-fatter, amplifier non-linearities, etc. make the transformation weakly non-linear, but these effects are small. Moreover, the shape of the PSF varies across the focal plane: in this work we assume that the region of interest is always small enough that the PSF can be assumed as constant.

Since convolution is a linear operation, it is formally invertable. However, this process is not stable. In Fourier space, convolution becomes multiplication and thus Equation 1 becomes

$$I_i(k) = I_{gt,i}(k) \cdot \text{PSF}_i(k) + N_i(k), \quad (2)$$

In this space, the naive inversion is therefore given by

$$\text{PSF}_i^{-1} I_i(k) = I_{gt,i}(k) + \frac{N_i(k)}{\text{PSF}(k)}, \quad (3)$$

Since the noise is added *after* convolution with the PSF, the recovery of spatially high-frequency modes that were blurred by the PSF are replaced with a blown-up noise that dominates the output image. In other words, the spatially high-frequency modes in the original image are truly lost information and therefore cannot be recovered. The deconvolution thus needs to be regularized.

One of the classical regularization techniques is Wiener deconvolution. In this technique, we deconvolve the modes which have high signal-to-noise and suppress those that are noise dominated. In Fourier space, the deconvolution operator can be written as (dropping the band subscripts for clarity):

$$\text{WD} = \frac{P_s(k)}{P_s(k) + P_n(k)\text{PSF}^{-2}(k)} \text{PSF}^{-1}(k), \quad (4)$$

where  $P_s(k)$  and  $P_n(k)$  are spectral densities of signal and noise respectively. Wiener deconvolution can be formally derived as Wiener filtering applied to the deconvolution problem. It is the filter that minimizes the mean-square error between the input and the truth, assuming we do not have any knowledge about the statistical properties of the truth images.

The Deep Wiener Deconvolution Network is a neural network extension of Wiener Deconvolution, which we describe in the following section.

## 3. BAND-WISE DEEP WIENER DECONVOLUTION NETWORK

The network utilized in this paper is an extension of Deep Wiener Deconvolution Network (DWDN, Dong et al. 2020). DWDN provides a brand new solution for the non-blind image deblurring problems. Instead of denoising and deconvolving the image in the image space like the existing methods do, DWDN applies Wiener Deconvolution explicitly in the feature space. As a simple but effective integration for classical Wiener Deconvolution and deep learning, DWDN achieves outstanding performance with fewer artifacts in solving the non-blind image deblurring problem. It contains two components, the feature-based Wiener deconvolution module and a multi-scale feature refinement module, where the former carries out the deconvolution process and the latter restores high-quality images using features from the previous module. The procedure is given by

$$h^l = \mathcal{F}^{-1} \left( \frac{\overline{\text{PSF}(k)}}{\overline{\text{PSF}(k)\text{PSF}(k)} + \frac{s_n^n}{s_i^x}} \right) \quad (5)$$

$$\hat{I} = \mathcal{R}(h^1, \dots, h^L)$$

where  $h^l$  is the deconvolved feature for  $l$ -th channel and  $l \in [1, \dots, L]$ .  $L$  denotes the number of channels of the feature.  $\mathcal{F}$  refers to discrete Fourier transformation and  $\overline{\text{PSF}(k)}$  is the complex conjugate of  $\text{PSF}(k)$ .  $s_n^n$  and  $s_i^x$  are the variance and standard deviation of  $l$ -th channel of the features in latent space for noise and input image separately which can be estimated by blurred features and mean-filtered features.  $\mathcal{R}$  refers to the feature refinement module and  $\hat{I}$  denotes the output of the model.

A restriction that limits the direct use of DWDN on astronomical images is that typically, for galaxy images, different bands have different PSFs. However, in DWDN, the feature maps extracted from the input have already

mixed up and no longer have distinguishable bands as the image does. Thus, we propose an enhanced variant of DWDN that can work on band-dependent PSFs. Figure 1 shows the architecture of our model. In order to apply feature-based deconvolution on different input bands separately, we parallel three deconvolution modules. The number of the deconvolution modules varies based on the number of bands in the input image and PSF. Each band of the input image with the corresponding PSF band will go through one of those modules to complete the feature-based deconvolution. Eq. 6 expresses the deconvolution for  $l$ -th feature channel in  $i$ -th deconvolution module

$$h_i^l = \mathcal{F}^{-1} \left( \frac{\overline{\text{PSF}_i(k)}}{\overline{\text{PSF}_i(k)\text{PSF}_i(k)} + \frac{s_{i,l}^n}{s_{i,l}^x}} \right) \quad (6)$$

$$H_i = \mathcal{C}[h_i^1, \dots, h_i^L] \quad (7)$$

The features will then be concatenated as Eq. 7, which means  $H_i$  is the output from  $i$ -th deconvolution module, namely, deconvolved features for  $i$ -th band of the input image and PSF. The deconvolved features will then be passed into the second module as shown in Eq. 8 with  $C$  denoting the total number of deconvolution modules. We keep the refining module  $\mathcal{R}$  the same except that the number of channels of its input feature is  $C$  times that of the original DWDN because of the concatenation. In this way, the different bands of the input image will execute their own deep Wiener deconvolution and the deconvolved features are utilized to restore the clean images.

$$\hat{I} = \mathcal{R}(H_1, \dots, H_C) \quad (8)$$

Specifically, there are  $C = 3$  parallel deconvolution modules. Each module is composed of  $m$  residual blocks following a convolution layer and each residual block contains 2 convolutional layers. The multi-scale feature refinement module starts from the top of a coarse-to-fine pyramid-like feature group using bicubic downsampling. The features will go through an encoder-decoder network with skipping connections to restore the clean image. In the refinement module, the output from the previous level will also be upsampled and utilized for the computation of the next level. The output of the final level will have the same shape as the original input image and is the final prediction from the model.

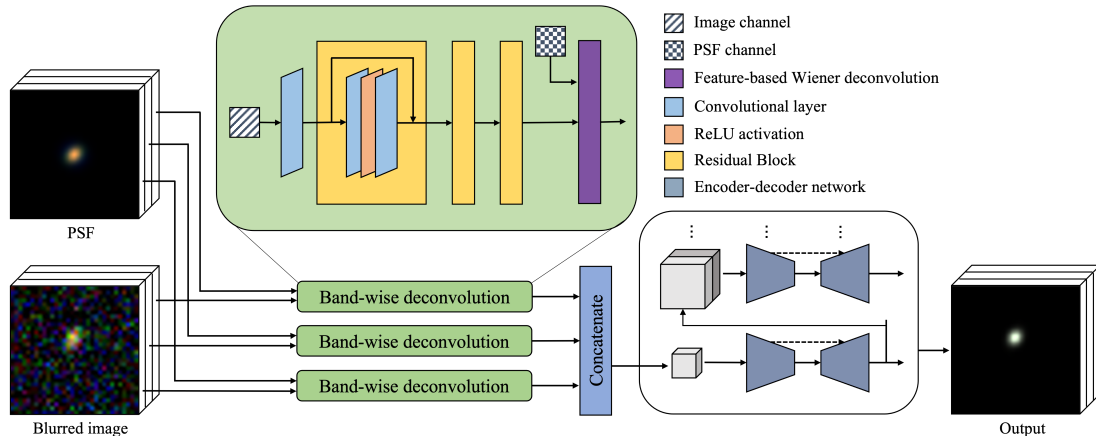


FIG. 1.— The framework of the model used in this work. The three channel-wise deconvolution modules share the same architecture. The feature refinement module contains convolution-based encoder-decoder network for multiple levels. The kernel size is  $5 \times 5$  for all convolutional layers.

#### 4. CUSTOM LOSS FUNCTION

In majority of image analysis problems, the networks are trained with one of the standard loss-functions that encode some intuitive notion of similarity between the true and reconstructed images. Typical examples include  $\ell_1$  (Least Absolute Deviation, LAD, Dodge 2008),  $\ell_2$  (Least Square Errors, LSE, Merriman 1877, Stigler 1981) loss functions<sup>1</sup>, and cross-entropy functions (binary, categorical, sparse categorical etc., Murphy 2012)<sup>2</sup>.

However, in astronomical image analysis we are interested in particular properties of the output image. In fact the first few image moments described in the next section naturally describe the astronomical quantities of interest: object brightness, position and shape. It is therefore natural to include them into the loss function to be minimized during training – this way we ask the neural network to focus explicitly on the quantities of interest. We will describe this non-standard training procedure next.

<sup>1</sup> L1 & L2 functions are also used for regularization, in order to prevent overfitting.

<sup>2</sup> <https://keras.io/>

## 4.1. Quantities of interest

Let  $I_{ij}$  be the flux value in pixel  $(i, j)$ . We define raw moments as

$$M_{pq}(I) = \sum_{x=1}^W \sum_{y=1}^H x^p y^q I_{x,y} \quad (9)$$

The following quantities are of interest:

$M_{00}$	Total flux	
$\langle x \rangle = \frac{M_{10}}{M_{00}}$	astrometric position $x$	
$\langle y \rangle = \frac{M_{01}}{M_{00}}$	astrometric position $y$	
$\mu_{20} = \frac{M_{20}}{M_{00}} - \langle x \rangle^2$	second central moment $x^2$	
$\mu_{11} = \frac{M_{11}}{M_{00}} - \langle x \rangle \langle y \rangle$	second central moment $xy$	(10)
$\mu_{02} = \frac{M_{02}}{M_{00}} - \langle y \rangle^2$	second central moment $y^2$	
$e_1 = \frac{\mu_{20} - \mu_{02}}{\mu_{20} + \mu_{02}}$	+ ellipticity component	
$e_2 = \frac{2\mu_{11}}{\mu_{20} + \mu_{02}}$	× ellipticity component	

These quantities can be trivially calculated from a noise-less image in a way that enable their use in loss functions.

## 4.2. Training procedure and loss function

The model is trained in an end-to-end manner and it contains two phases. In the first phase, the model is pre-trained to acquire the ability to deblur and produce a reasonable prediction as the output, while in the second phase, the model is fine-tuned with a more complex loss including the quantities listed in Section 4.1 for a more accurate description of the galaxy.

The loss function for the first phase is formulated in Eq. 13. The first part of the loss is  $\ell_1$ -norm between the output image and the ground truth as shown in Eq. 11. We also include the difference of the total flux in this phase written as Eq. 12 as the image properties described are close. In Eq. 11,  $f$  is the network,  $I$  and  $I_{gt}$  refer to the blurred input and the ground truth separately.  $\lambda_0$  controls the trade-off between these two parts.

$$\mathcal{L}_{\ell_1} = \frac{1}{WHC} \sum_{c=1}^C \sum_{x=1}^W \sum_{y=1}^H |f(I)_{x,y,c} - (I_{gt})_{x,y,c}| \quad (11)$$

$$\mathcal{L}_{M_{00}} = \frac{1}{C} \sum_{c=1}^C |M_{00}(f(I)) - M_{00}(I_{gt})| \quad (12)$$

$$\mathcal{L}_1(I, I_{gt}) = \mathcal{L}_{\ell_1} + \lambda_0 \mathcal{L}_{M_{00}} \quad (13)$$

In the second phase, in addition to  $\mathcal{L}_{\ell_1}$  and  $\mathcal{L}_{M_{00}}$ , the astrometric position  $\langle x \rangle$  and  $\langle y \rangle$ , the second-order central moments  $\mu_{11}$ ,  $\mu_{20}$ ,  $\mu_{02}$  are utilized to fine-tune the model. The quantities are defined in Section 4.1 and the loss for these quantities has the same form as Eq. 12. Thus, the total loss for the second phase can be written as Eq. 14 where  $\lambda$ 's are the weights for the different terms.

$$\mathcal{L}_2(I, I_{gt}) = \mathcal{L}_{\ell_1} + \lambda_0 \mathcal{L}_{M_{00}} + \lambda_1 \mathcal{L}_{\langle x \rangle} + \lambda_2 \mathcal{L}_{\langle y \rangle} + \lambda_3 \mathcal{L}_{\mu_{11}} + \lambda_4 \mathcal{L}_{\mu_{20}} + \lambda_5 \mathcal{L}_{\mu_{02}} \quad (14)$$

Values of  $\lambda_i$  parameters are manually adjusted so that those terms are subdominant, but not negligible compared to the dominant  $\ell_1$  loss.

## 5. TRAINING AND TESTING DATA

The dataset used in this work was generated using `WeakLensingDeblending` package<sup>3</sup> developed in order to test the shear measurement of weak lensing by LSST Data Management. From the galaxy catalog class `FixedGalaxyCatalog`, composite exponential galaxy images of single galaxies are simulated in `g`, `r` and `i` bands with single exposures per band. The PSFs are generated as follows. First, for each PSF we draw the value of FWHM (full width at half maximum) uniformly between 0.4 and 1.0 arcsec. The two components of the PSF are assigned the drawn FWHM further perturbed by zero-mean Gaussian variates with  $\sigma = 0.1$  arcsec. Object and PSFs are rendered using the industry standard `galsim` package (Rowe et al. (2015)). For each galaxy, a noisy image, a truth image and a PSF image are generated as a stack of the three aforementioned bands. Since our objective is to ascertain the influence of

<sup>3</sup> <https://github.com/LSSTDESC/WeakLensingDeblending/>

incorporating PSF in neural networks for denoising astronomical images, we have set the shear to be zero. Moreover, we incorporated a signal-to-noise (SNR) cut of  $> 10$  with the SNR calculated as,

$$SNR = \sqrt{\sum_{pixels} \frac{truth^2}{\sigma^2}} \quad (15)$$

where `truth` is the truth image and  $\sigma^2$  is the noise variance. The 100,000 images thus generated for each of the three categories (truth, noisy and PSF) have dimensions of  $35 \times 35 \times 3$ .

The entire dataset is divided into training and test sets where the training set contains 90,000 images, while the test set contains 10,000 images. Each image is sized  $32 \times 32 \times 3$  and normalized to  $[0, 1]$  by dividing its overall maximum pixel value so that colors are preserved. Exactly the same renormalization factor is applied to both input and output images. During testing, in order to get the accurate performance of the model, the prediction from the network are rescaled back by exactly same factor which allows a direct comparison with the ground truth.

## 6. RESULTS

### 6.1. Implementation and comparison models

In our framework, each band-wise deconvolution modules contains  $m = 3$  residual blocks. We adopt Adam optimizer (Kingma & Ba 2014) to update the parameters in the model and the batch size is 128. During the first phase of the training process, the model is trained for 80 epochs with learning rate as  $10^{-4}$ . In the second phase, we fine-tune the model for 10 epochs and the learning rate is set to  $10^{-5}$ . The weights for moment-related loss are manually as following:  $\lambda_{0,1,2} = 0.01$ ,  $\lambda_3 = 0.002$  and  $\lambda_{4,5} = 0.001$ . Those parameters are chosen to 1) keep the dominance of the  $\ell_1$ -loss and 2) scale the loss terms to be comparable.

In order to evaluate the performance of our model we train 4 different models:

- The fiducial model as explained in the text;
- The *Average PSF* model, where the training and testing datasets remain the same, but instead of fitting actual per-image PSF to the network, we freeze the PSF to its average shape. This allows us to explore the information gain coming from knowledge of the actual PSF
- The  $\ell_1$  *loss only* model, where training is not fine-tuned with custom loss function;
- The *Gaussian regularization* model where Wiener deconvolution formula is replaced with a different regularization as described in Section 6.2.2.

### 6.2. Evaluation

In most tests we split the sample into three categories by the value of  $M_{00}$  as a proxy for signal-to-noise. Fig. 2 visualizes the performance of the trained model on the testing set. We select one example from samples with low, medium and high  $M_{00}$  separately. From the results, our deblurring model can recover the morphological and color information for images under different conditions, even for images with low fluxes. It can also be observed that the model performs better on images with higher fluxes. We will analyse in detail in the following sections.

We first use some standard metrics such as the peak signal-to-noise ratio (PSNR) and the structural similarity index (SSIM) to evaluate the quality of images recovered from our model compared with the true images. PSNR, as a measurement of peak error between the original and reconstructed images, is the ratio between the maximum of the true image and the mean squared error of the true and recovered images in logarithmic decibel scale. The expression for PSNR is in Eq. 16. SSIM (Wang et al. 2004) evaluates the similarity between two images based on quantities related to visible structures in the image such as mean, variance and covariance. The SSIM is formulated as Eq. 17. We use default settings for constants  $c_1$  and  $c_2$ . A higher PSNR or SSIM value represents better image recovery.

$$PSNR(\text{dB}) = 20 \cdot \log_{10}(\text{MAX}) - 10 \cdot \log_{10}(\text{MSE}) \quad (16)$$

$$SSIM = \frac{(2\mu_x\mu_y + c_1)(2\sigma_{xy} + c_2)}{(\mu_x^2 + \mu_y^2 + c_1)(\sigma_x^2 + \sigma_y^2 + c_2)} \quad (17)$$

The evaluation of our fiducial model and the three comparison models are listed in Table 1, including the mean and median among the testing set. The best results are from the model with accurate PSF and moment loss. Specifically, by comparison between the first and third columns in the table, we can conclude that the moment-related loss terms help improve the performance, reflected by a higher PSNR and SSIM value, but the improvement is modest. The results from models with accurate PSF and average PSF also demonstrate that the quality of the prediction will get degraded if an accurate PSF is not provided for each image again with surprisingly modest improvements.

	Accurate PSF		Average PSF		Accurate PSF ( $\ell_1$ loss)			Gaussian regularization	
	Mean	Median	Mean	Median	Mean	Median	Mean	Median	
PSNR	46.408	45.951	45.172	44.991	46.314	45.477	46.273	45.724	
1-SSIM	0.011	0.006	0.012	0.007	0.011	0.007	0.011	0.006	

TABLE 1  
PSNR(DB) AND SSIM

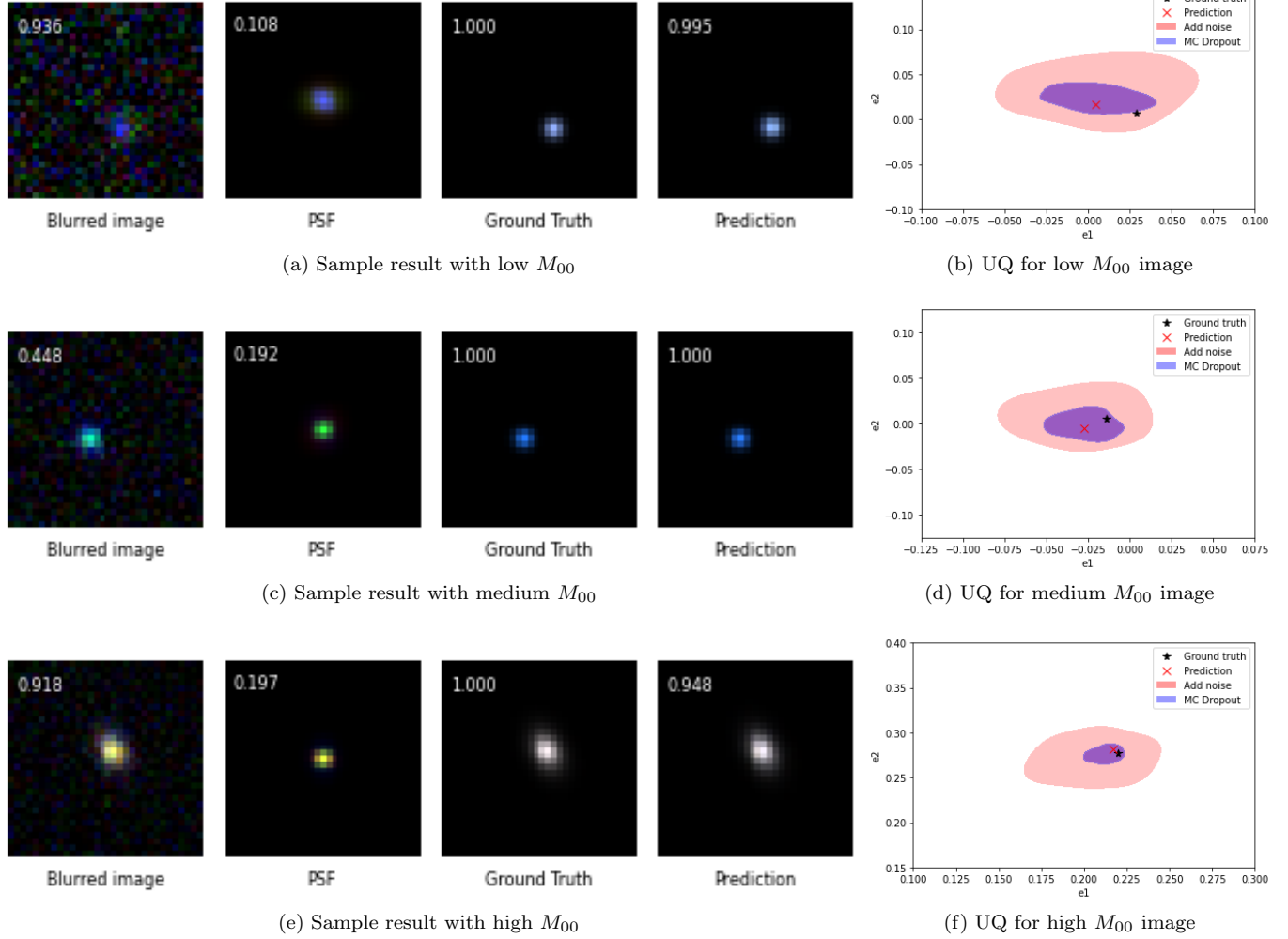


FIG. 2.— Visualization of typical results.

	Accurate PSF			Average PSF			Accurate PSF ( $\ell_1$ loss)			Gaussian regularization		
	Mean	Variance	RMS	Mean	Variance	RMS	Mean	Variance	RMS	Mean	Variance	RMS
$M_{00}$	0.015	131.416	11.464	-0.053	129.831	11.394	-1.142	259.151	16.139	-0.484	124.569	11.172
$\langle x \rangle$	0.011	0.046	0.214	0.003	0.045	0.212	0.005	0.050	0.224	0.002	0.050	0.225
$\langle y \rangle$	0.009	0.045	0.213	0.017	0.044	0.211	0.005	0.050	0.223	0.011	0.049	0.223
$\mu_{20}$	-0.038	2.577	1.606	-0.160	2.867	1.701	-0.222	2.555	1.614	0.103	2.469	1.574
$\mu_{02}$	-0.096	2.712	1.650	-0.169	2.977	1.734	-0.255	2.655	1.649	0.072	2.566	1.604
$\mu_{11}$	-0.017	0.413	0.643	-0.007	0.491	0.701	-0.016	0.466	0.683	-0.001	0.440	0.664
$e_1$	0.007	0.020	0.140	-0.003	0.024	0.154	0.003	0.023	0.151	0.003	0.018	0.134
$e_2$	-0.002	0.020	0.142	0.005	0.039	0.198	-0.003	0.024	0.154	0.004	0.019	0.137
$\ e\ $	0.155	0.016	0.152	0.179	0.031	0.202	0.171	0.017	0.138	0.153	0.013	0.150

TABLE 2  
DIFFERENCE OF MOMENTS BETWEEN PREDICTED IMAGES AND GROUND TRUTH.

### 6.2.1. Recovery of astronomical quantities

	Accurate PSF			Average PSF			Accurate PSF ( $\ell_1$ loss)			Gaussian regularization		
	Mean	Variance	RMS	Mean	Variance	RMS	Mean	Variance	RMS	Mean	Variance	RMS
$M_{00}$	-0.0812	377.2651	19.4235	-0.1535	371.7244	19.2808	-2.7519	755.9718	27.6323	-1.5596	355.4639	18.9182
$\langle x \rangle$	0.0085	0.0097	0.0989	-0.0008	0.0094	0.0972	0.0032	0.0083	0.0910	-0.0035	0.0081	0.0901
$\langle y \rangle$	0.0098	0.0095	0.0978	0.0200	0.0102	0.1028	0.0043	0.0092	0.0962	0.0097	0.0094	0.0975
$\mu_{20}$	-0.0512	1.7330	1.3174	-0.1423	2.0305	1.4320	-0.1659	1.6007	1.2760	-0.0732	1.5690	1.2547
$\mu_{02}$	-0.1310	1.8618	1.3708	-0.1752	2.2053	1.4953	-0.2122	1.7462	1.3384	-0.1126	1.6981	1.3080
$\mu_{11}$	-0.0106	0.3259	0.5709	0.0136	0.4834	0.6954	0.0013	0.3466	0.5887	0.0217	0.3557	0.5968
$e_1$	0.0050	0.0051	0.0716	-0.0007	0.0111	0.1054	0.0037	0.0055	0.0743	0.0018	0.0052	0.0720
$e_2$	-0.0003	0.0048	0.0689	0.0059	0.0111	0.1054	0.0012	0.0054	0.0736	0.0051	0.0049	0.0700
$\ e\ $	0.0790	0.0036	0.0746	0.1215	0.0074	0.1035	0.0806	0.0044	0.0755	0.0804	0.0036	0.0768

TABLE 3  
THE SAME AS TABLE 2, BUT ONLY FOR HIGH  $M_{00}$ .

	Accurate PSF			Average PSF			Accurate PSF ( $\ell_1$ loss)			Gaussian regularization		
	Mean	Variance	RMS	Mean	Variance	RMS	Mean	Variance	RMS	Mean	Variance	RMS
r-b	-0.014	0.063	0.251	-0.020	0.074	0.273	0.001	0.062	0.250	-0.001	0.061	0.247
b-g	0.020	0.039	0.200	0.023	0.046	0.216	0.005	0.039	0.197	0.008	0.040	0.201
g-r	-0.006	0.021	0.145	-0.003	0.025	0.159	-0.006	0.022	0.148	-0.007	0.022	0.148

TABLE 4  
ASTRONOMICAL MAGNITUDE DIFFERENCE BETWEEN TWO BANDS.

Table 2 presents the difference between the prediction from the model and ground truth image for the astronomical quantities of interest. These values are averaged over the three available bands. For our fiducial network, the relevant scatter plots can also be found in Figure 3. We find that across the noise levels, the networks correctly recover the quantities of interest. The results nicely scatter around the  $x = y$  line with no obvious bias for the total flux, first moments (astrometric positions) and second moments. Ellipticity suffers from a small bias, where the network tends to preferably make objects less round. This effect is observed for both  $e_1$  and  $e_2$ . To understand this effect better we have split objects by signal-to-noise and re-plotted the ellipticity histograms in the Figure 4. Here we see that high signal-to-noise objects have their shapes recovered without bias, while there is an emergence of "multiplicative" bias for low signal-to-noise where measured ellipticities are systematically low.

Next we want to study how much information we are getting by using a per-band known PSF. The equivalent of Figure 4 for the model with average PSF is plotted in Figure 5. We see essentially the same structure, but the scatter around the mean is somewhat higher. This is confirmed in Table 2, where RMS (root mean square) errors when using average PSF (2nd column) are systematically larger by about 5 – 10% compared to those of the fiducial network for ellipticity and second moments. We also find that the error on the astrometries are not affected by knowledge of the true PSF – this makes sense because our PSFs are Gaussian with zero mean and therefore using a wrong PSF to deconvolve the image is not going to affect its central position. What is somewhat more surprising is that the error on the object flux also seems to be unchanged between the two cases.

To investigate this further we turn to color recovery. We define object colors to be the logarithm of the ratio for  $M_{00}$  between two channels written as

$$r - b = -2.5 \times \log \frac{(M_{00})_r}{(M_{00})_b}. \quad (18)$$

Thus defined color approximately corresponds to an astronomer's color, which is the astronomical magnitude difference between two bands. Results are shown in Table 4. We see 10% improvement in color recovery when the real rather than average PSF is used. The reason for this is a band dependent PSF, which can artificially change the color of an object. This is also illustrated in the Figure 2, where we see that the object in the blurred image is of a different color than the object in the ground truth image.

### 6.2.2. Recovery of shapes and its biases

We next study the performance of our network in removing the subtle biases that remain in the prediction. In particular, we want to study the remaining contamination by the PSF shape. Our main motivation is to understand whether such methods could ever be used for weak lensing applications, where residual contamination with the PSF leads to the so-called additive bias (see Mandelbaum (2018) and references there-in for an in-depth review). In short if the shape of galaxy remains correlated with the PSF after the convolution, then this PSF shape will leak into shear estimation and lead to shape correlations that can mimic real weak gravitational signal.

The true galaxy ellipticities are uncorrelated with PSF shapes, but since the observed image is a convolution of the PSF with true shape, the resulting predicted image ellipticities might still correlate with the PSF shape. On the other hand, if a measurement is perfect, the predicted ellipticities should correlated perfectly with true ones. To quantify this effect, we define the following correlations

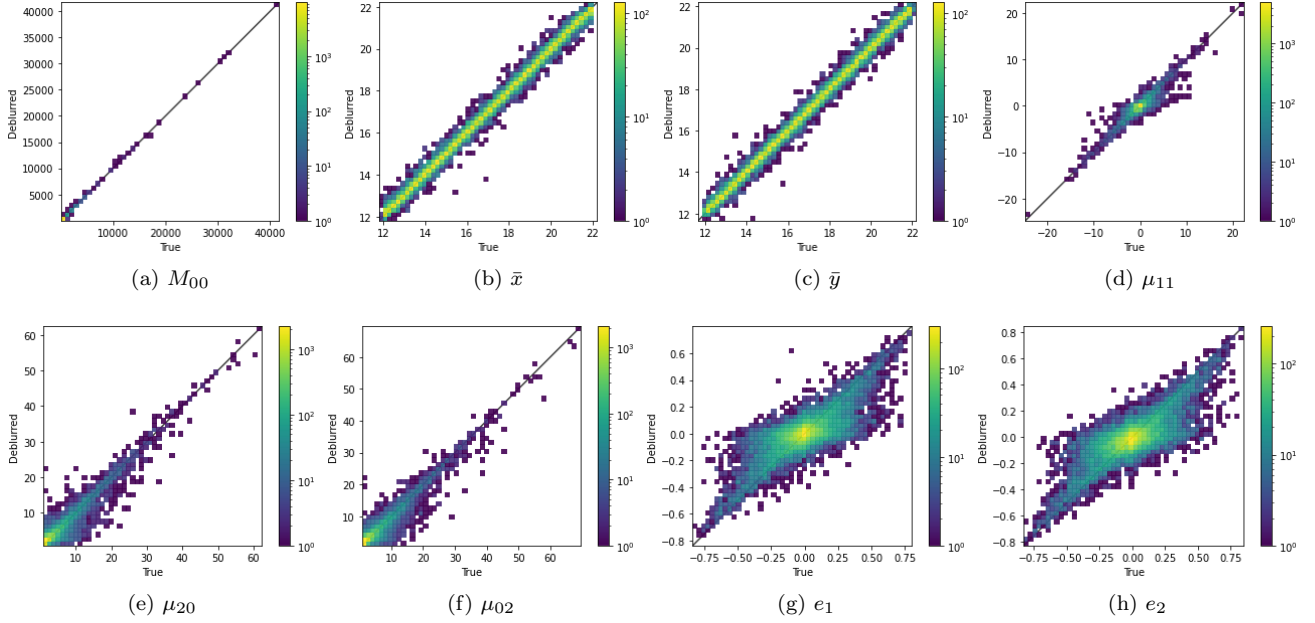


FIG. 3.— 2-d histograms for moment recovery from model trained with accurate PSF. Different panels are for different quantities as indicated. The  $x$  axis was calculated on the true image and the  $y$  axis on the recovered image. The density of points is represented with color. Note that the color scaling is logarithmic to bring out the outliers.

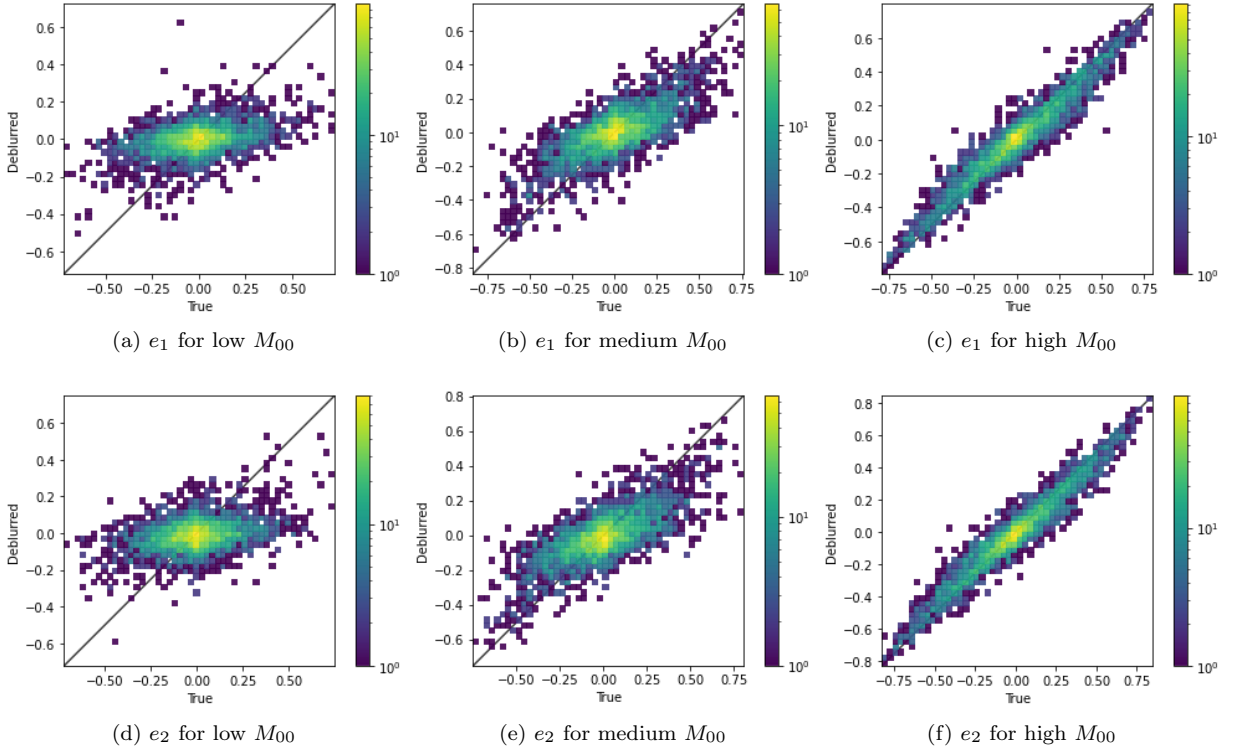


FIG. 4.— 2D distributions of ellipticity recovery split by signal-to-noise for the fiducial model.

$$\xi_{\text{PSF}} = \frac{\langle \mathbf{e}_{\text{PSF}} \cdot \mathbf{e}_{\text{pred}} \rangle}{\langle |\mathbf{e}_{\text{PSF}}| |\mathbf{e}_{\text{pred}}| \rangle}, \quad (19)$$

$$\xi_{\text{true}} = \frac{\langle \mathbf{e}_{\text{true}} \cdot \mathbf{e}_{\text{pred}} \rangle}{\langle |\mathbf{e}_{\text{true}}| |\mathbf{e}_{\text{pred}}| \rangle}, \quad (20)$$

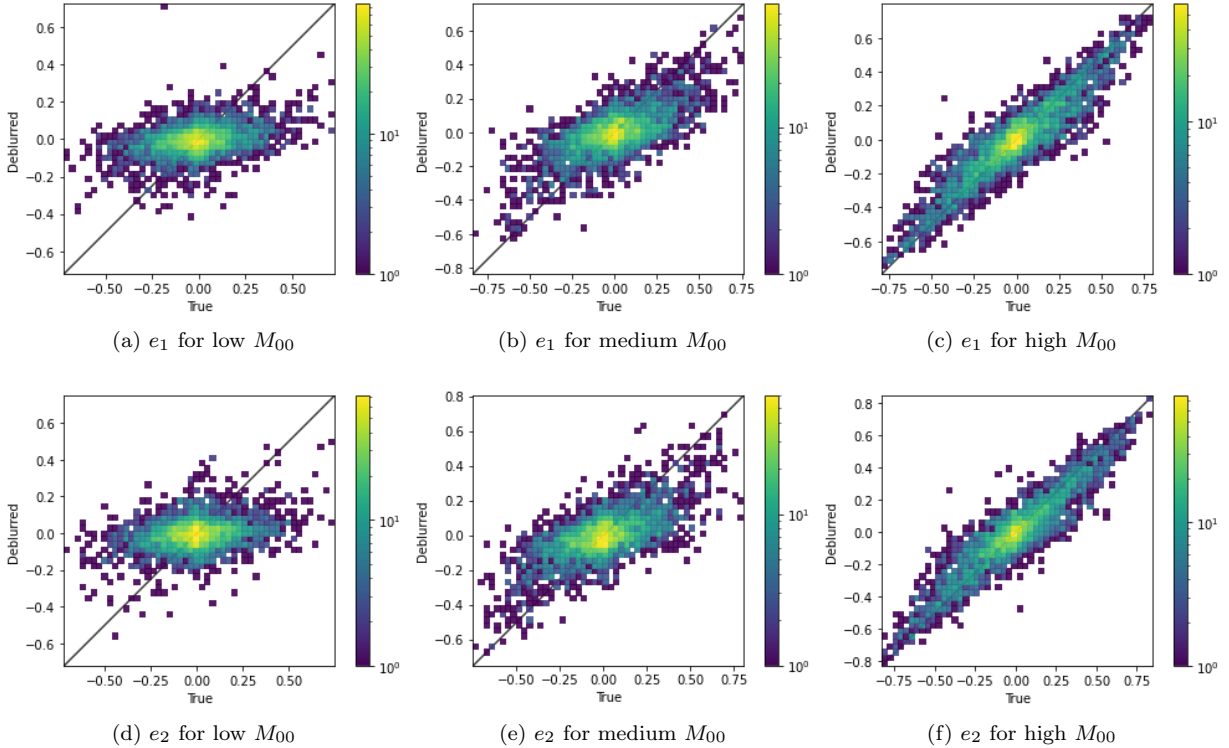


FIG. 5.— 2D distributions of ellipticity recovery split by signal-to-noise for model trained with average PSF.

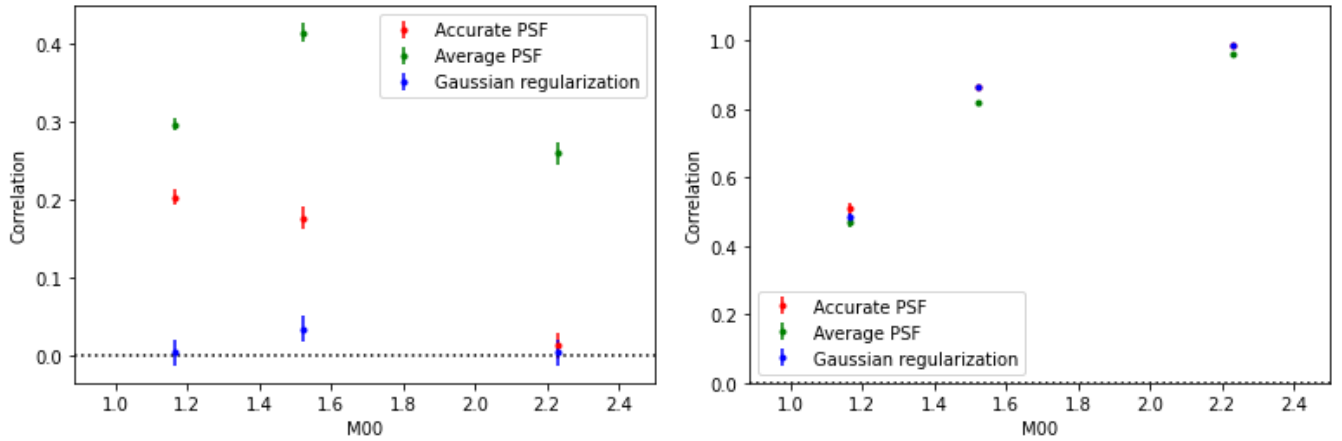


FIG. 6.— Cross correlation of the network output ellipticities with the PSF (left) and with the true image ellipticities (right).

where averages are calculated by simply averaging the data in the test dataset. Note that since individual ellipticities of either PSF, true galaxy image or predicted galaxy image can reach zero, we average the numerator and denominator separately. In an ideal case, we expect the predicted image to remove any trace of PSF from the resulting image, so  $\xi_{\text{PSF}} = 0$ . However, this could also be achieved by making all objects round (i.e.  $e_{\text{pred}} = 0$  for every objects). Therefore we also look at the correlation with the true value, which should be, in the ideal case perfect, i.e  $\xi_{\text{true}} = 1$ .

Results of this exercise are plotted in the Figure 6. We see that our fiducial case (denoted "Accurate PSF" and plotted red) performs better than the "Average PSF" case across all signal-to-noise levels. The cross-correlation with PSF is significantly lower and the cross-correlation with the truth significantly higher. We conclude that the deconvolution is taking place, albeit imperfectly: although the network does successfully decorrelate PSF in the high SNR regime, it still contains significant contamination in the lower SNR regime.

In order to improve upon this, we explore another version of deconvolution in which we replace the Wiener filter Equation 4 with a modified term, which we refer to as "Gaussian Regularization":

$$\text{WD}^{\text{GaussReg}} = \frac{P_s(k)}{P_s(k) + P_n(k)G^{-2}(k)} \text{PSF}^{-1}(k), \quad (21)$$

In other words, the PSF is linearly deconvolved from the noisy image, but the resulting image is then regularized with a circular Gaussian roughly the size of the PSF. In the original formulation of the Wiener filter, modes are anisotropically regularized, taking into account that the anisotropic PSF has destroyed more information in some directions than the others. However, the result is that the PSF shape can sneak back into the resulting image. The Gaussian regularization tries to prevent this at the expense of formally decreased optimality, i.e. the resulting process is now manifesting a worse than minimum variance solution. We choose a Gaussian whose size is close to typical PSF size and have explicitly demonstrated that the results are largely insensitive to the precise choice of this kernel, if the network is retrained.

In our tests, however, this method seems to perform pretty well. In Figure 6, we see that the Gaussian regularization model performs significantly better than our fiducial network with no evidence of PSF correlation at no loss in correlation with the truth. In our main results presented in Tables 2 and 3, we see that the Gaussian regularization performs essentially as well as the fiducial model within the noise and that while individual RMS values scatter favouring one or the other method, there is no clear winner.

### 6.3. Uncertainty quantification (UQ)

Like majority of the deep learning frameworks, the DWDN is also a point-prediction method, i.e., the predictions in the network are not associated with error estimates. A large number of UQ approaches are currently applied in the context of AI (artificial intelligence) applications in physics (Chen et al. 2022), with associated advantages and disadvantages based on the problem. For instance, a sampling over the network weights (Neal 2012) or an ensemble-based error estimate (Lakshminarayanan et al. 2016) may be computationally expensive in our problem, where the individual model training requires 25.5 hours on one Nvidia V100 GPU with 32GB memory.

In this paper, we perform a two-fold treatment of uncertainty. The first one aims at estimating the model uncertainties, where we quantify the fluctuations in the predicted deconvolved images due to imperfect model training. Second, we quantify the uncertainty propagated due to noisy input data during the testing phase. Both these treatments are approximations aimed at obtaining a rudimentary understanding of the confidence intervals of our methods, within reasonable computational budgets. In applications involving real observations, several systematic effects may have to be considered in a greater detail.

#### 6.3.1. Model uncertainty using Monte Carlo methods

For quantifying model uncertainties, we choose the UQ technique of Monte Carlo (MC) Dropout, that provides approximates errors with little computational overhead and minimal changes to the DWDN architecture. The implementation of MC Dropout is as follows: First, we train a DWDN without any UQ considerations to obtain an optimized denoising architecture. Note that the custom losses in 3 are all based on image outputs, and do not consider error estimations. Next, we consider an ensemble of  $N_{tot}$  such DWDNs, only differing from each other by a fraction of trained neurons that are re-initialized to a random value. This fraction of weights that are randomized (or ‘dropped-out’) is dictated by the dropout rate  $d$ . Using the base architecture shown in Figure 1 with dropout rate  $d$ , we obtain this ensemble of  $N_{tot}$  networks. Since the Deep Neural Networks are over-parametrized, a small number of randomized weights will only result in small fluctuations in the deconvolved output images.

When a validation image  $I$  is forward propagated through each network in the ensemble, they provide individual predictions for the deconvolved images  $f^k(I)_{x,y,c}$ , where  $k = 0, 1, \dots, N_{tot}$ . These individual predictions  $f^k(I)_{x,y,c}$  are different from each other due to the fact that a different fraction of their network parameters are dropped-out. The mean  $\langle f(I) \rangle$  and variance  $\sigma_f^2$  of all the individual predictions is calculated as shown in Eq. 22.

$$\begin{aligned} \langle f(I) \rangle &= \frac{1}{N_{tot}} \sum_{k=0}^{N_{tot}} f^k(I)_{x,y,c}, \\ \sigma_f^2 &= \frac{1}{N_{tot}} \sum_{k=0}^{N_{tot}} [f^k(I)_{x,y,c} - \langle f(I) \rangle]^2 \end{aligned} \tag{22}$$

These aggregate mean and variance will be considered as the UQ prediction from the ensemble. Since the estimates are only computed during the deployment time, there is no change in the network training or associated computational costs.

#### 6.3.2. Statistical uncertainty due to noisy image inputs

In addition to model uncertainty, which corresponds to systematic error in the language of physicists, any observation has also noise or random uncertainty. Since the neural network results (without the MC Dropout at inference) are point estimates, one would ideally process the same image with multiple noise realizations to estimate the noise in any derived quantities. Since this is impossible, we instead generate  $N_{tot}$  images with additional noise drawn from the same distribution as the real noise and run those through the network. These now form an ensemble from which a noise estimate on the derived quantities can be formed. Since these images now have double the noise variance, the result is strictly speaking an overestimate of measurement uncertainty.

In the experiment,  $N_{tot} = 200$  for both approaches and dropout rate  $d = 0.2$ . Results of these two techniques are presented in the right panel of Figure 2. We see that the truth is always within the estimated uncertainty region,

whose size is likely overestimated. We also see that the size of the statistical uncertainty decreases with increasing SNR, but interestingly the size of the systematic uncertainty also somewhat shrinks with an increasing SNR. In other words, as the SNR increases, the network seems to internally produce more consistent results. Formally investigating these statistical properties of this uncertainty quantification exceeds the scope of this paper.

## 7. DISCUSSION & CONCLUSIONS

Despite numerous applications of neural networks to astronomical image analysis, the problem of using the information from the known, band dependent and relatively large PSF has not been addressed directly. While the PSF information is always taken into account in classical image reduction, neural network applications so far usually assume a fixed PSF. This is problematic for several reasons. First, PSF can undergo weather induced changes in size and shape from observation to observation and from band to band. This means that one cannot simply assume a constant PSF or that the neural network will have to be retrained for every new sets of observations. Similarly, the large number of possible combinations given band shape and size changes makes building a grid of models impractical. Therefore, a method is required that is capable of taking the PSF shape directly as input.

The naively obvious approach of simply adding a PSF image to a standard convolutional neural network would not work. Convolutional network inherently assumes that information is localized in the image coordinate space, while the relation between the PSF image, ground truth and observed image is convolutional. We therefore chose a state-of-the-art non-blind deconvolution method called Deep Wiener Deconvolution Network. We have trained the network to be able to deconvolve and denoise individual galaxy images. While this approach is not yet ready for the prime-time, it illustrates a technique that could be used in more complete neural-network based approaches to astronomical image analysis.

Our results can be summarized as follows:

- The network is correctly using information from the provided PSF shape. We checked this by retraining the same model with the mean PSF shape instead and obtained consistently worse results.
- Improvement is the largest for the shape recovery and for objects with higher SNR. In that case, the SNR improvement can be up to 30%. We also find that while the noise on individual fluxes is not affected, the color recovery is about 10% better with using actual PSF information.
- Without using PSF shape, there is simply no information in the resulting image to disentangle the effects of the PSF shape from the intrinsic image ellipticity. We have found that using our fiducial network, the correlation between the resulting image and PSF is suppressed by 30%, 50% and  $> 80\%$  compared to network that does not know about PSF. However, the correlations are still significant at lower SNR. This has led us to create an alternative network with a Gaussian regularization that performs as well as fiducial network on most tests, but completely removes residual correlations with the PSF.

We have experimented with custom loss functions with mixed results. In particular, in addition to the standard pixel-wise  $\ell_1$  loss, we have added loss functions that attempt to force the network to improve on the quantities that are of interest to astronomers. When the weight of those terms was significant, the training became unstable. When they are sufficiently suppressed to enable stable learning, the improvements are modest, but significant at low SNR. We find the largest improvement in flux recovery.

Finally, we have investigated methods to understand both the statistical and systematic errors and found that we can correctly quantify the uncertainty in network performance.

The main limitation of the current work is that the network was trained and tested with a single object in each frame. As a result, the network would perform exceptionally well down to unrealistically low SNR (which forced us to impose a SNR cut). The main extension of this work would therefore be to test our approach on images that contain both multiple galaxies in the frame as well as no-galaxies with correct rates and thus use the system as a first step in object detection and deblending.

## ACKNOWLEDGEMENTS

We thank Erin Sheldon for useful discussions. This material is partly based upon the work supported by the U.S. Department of Energy, Office of Science, Office of Advanced Scientific Computing Research and Office of High Energy Physics, Scientific Discovery through Advanced Computing (SciDAC) program on "Accelerating HEP Science: Inference and Machine Learning at Extreme Scales". NR's work at Argonne National Laboratory was supported by the U.S. Department of Energy, Office of High Energy Physics. Argonne, a U.S. Department of Energy Office of Science Laboratory, is operated by UChicago Argonne LLC under contract no. DE-AC02-06CH11357.

## REFERENCES

- |   |   |
|---|---|
| <p>Abbott T. M. C., et al., 2018, <i>Phys. Rev. D</i>, 98, 043526</p> <p>Arcelin B., Doux C., Aubourg E., Roucelle C., LSST Dark Energy Science Collaboration 2021, <i>MNRAS</i>, 500, 531</p> <p>Boucaud A., et al., 2020, <i>Monthly Notices of the Royal Astronomical Society</i>, 491, 2481</p> | <p>Chen T. Y., Dey B., Ghosh A., Kagan M., Nord B., Ramachandra N., 2022, arXiv e-prints, p. arXiv:2208.03284</p> <p>Dodge Y., 2008, <i>Least Absolute Deviation Regression</i>. Springer, doi:10.1007/978-0-387-32833-1_225, <a href="https://doi.org/10.1007/978-0-387-32833-1_225">https://doi.org/10.1007/978-0-387-32833-1_225</a></p> |
|---|---|

- Dong J., Roth S., Schiele B., 2020, *Advances in Neural Information Processing Systems*, 33, 1048
- Green J., et al., 2012, arXiv e-prints, p. arXiv:1208.4012
- Hikage C., et al., 2019, *PASJ*, 71, 43
- Kingma D. P., Ba J., 2014, arXiv preprint arXiv:1412.6980
- LSST Science Collaboration et al., 2009, arXiv e-prints, p. arXiv:0912.0201
- Lakshminarayanan B., Pritzel A., Blundell C., 2016, arXiv e-prints, p. arXiv:1612.01474
- Mandelbaum R., 2018, *ARA&A*, 56, 393
- Merriman M., 1877, *A List of Writings Relating to the Method of Least Squares: With Historical and Critical Notes*. Transactions of the Connecticut Academy of Arts and Sciences, Academy, <https://books.google.co.in/books?id=8tIGAAAAYAAJ>
- Murphy K., 2012, *Machine Learning: A Probabilistic Perspective*. Adaptive Computation and Machine Learning series, MIT Press, <https://books.google.co.in/books?id=NZP6AQAAQBAJ>
- Neal R. M., 2012, *Bayesian learning for neural networks*. Vol. 118, Springer Science & Business Media
- Refregier A., Amara A., Kitching T. D., Rassat A., Scaramella R., Weller J., 2010, arXiv e-prints, p. arXiv:1001.0061
- Reiman D. M., Göhre B. E., 2019, *Monthly Notices of the Royal Astronomical Society*, 485
- Rowe B., et al., 2015, *Astronomy and Computing*, 10, 121
- Stigler S. M., 1981, *The Annals of Statistics*, 9, 465
- Wang Z., Bovik A. C., Sheikh H. R., Simoncelli E. P., 2004, *IEEE transactions on image processing*, 13, 600
- Wang H., Sreejith S., Slosar A., Lin Y., Yoo S., 2021, arXiv e-prints, p. arXiv:2109.09550